Analysis of the Retrieval Performance of 2-D Ionospheric Irregularity Maps in the Biomass Mission

Felipe Betancourt-Payan, *Graduate Student Member, IEEE*, Marc Rodriguez-Cassola, Pau Prats-Iraola, *Fellow, IEEE*, and Gerhard Krieger, *Fellow, IEEE*

***Abstract*— Low-frequency synthetic aperture radar (SAR) images are affected by trans-ionospheric propagation of the radar waves. The 2-D total electron content (TEC) maps can be obtained as a product of the ionospheric corrections, allowing for imaging of ionospheric irregularities at very high resolution and broader coverage compared to other sensing technologies (such as Global Navigation Satellite Systems (GNSS) and ionosondes). We analyze, in this article, the case of the Biomass mission and characterize the errors in the imaging of the ionosphere resulting from the calibration algorithms foreseen for its ground processor prototype: a Faraday rotation (FR)-based and an autofocus (AF) approach. The analysis relies on a turbulent power law Rino model for the perturbation of the ionosphere and the spectral behavior of the calibration algorithms. We also discuss the suitability of both approaches for image correction in different scenarios (varying signal-to-noise ratio (SNR) and geographic location).**

***Index Terms*— Autofocus (AF), Biomass, Faraday rotation (FR), ionosphere, synthetic aperture radar (SAR).**

I. Introduction

THE ionosphere is a region of the atmosphere that extends from ∼50 to 1000 km of altitude and consists of ionized plasma. It is a dispersive and dynamic medium for which the level of ionization and orientation of plasma depends on its interaction with the Earth's magnetic field and other factors like solar activity. Its state can be described by the free electron density. In most satellite applications, this electron density is measured as the integrated total electron content (TEC) between the platform and the ground. Several mechanisms have been developed over the years for sensing the ionosphere. Ionosonde techniques, for example, can provide vertical (or oblique, if operated in a bistatic mode) electron density profiles. This approach alone cannot provide global coverage despite increasing stations. On the other hand, Global Navigation Satellite Systems (GNSS) signals can be used for monitoring the spatially slow-changing ionosphere (background component) and, to some extent, continuous monitoring of ionospheric irregularities using the rate of TEC index (ROTI) [1], [2], able to provide average values to characterize the scintillation strength (e.g., using the S4 parameter) [3]. Even some approaches to imaging and tomography have been proposed [4]; however, they require large interpolations and smoothing (which lowers the resolution), and their capabilities are limited by the number and nonuniform distribution of the GNSS receivers that can be hundreds of kilometers apart.

The images of synthetic aperture radar (SAR) satellites are also affected by trans-ionospheric propagation, especially when operating at lower frequencies, and allow for sensing the ionosphere not with constant-global temporal coverage but with very high 2-D resolution. An example is the new SAR mission, Biomass from the European Space Agency (ESA), to be launched in 2024. Its main goal is quantifying the global forest Biomass, thus contributing to monitoring carbon fluxes and stocks. To reach this objective, it will be the first spaceborne SAR mission operating in P-band (435 MHz, ∼69-cm wavelength) with full polarimetry, allowing for both deep penetration into the forest canopies and good coherence for repeat-pass interferometry [5]. With a 12-m antenna, the SAR image resolution in azimuth for the single-look case is 6 m [6]. The ionosphere will leave its footprint in the images by introducing amplitude modulations, time delay, and phase advance in the radar echos (seen as geolocation and phase errors), as well as crosstalk among the polarimetric channels induced by Faraday rotation (FR). Of particular interest are the effects caused by ionospheric irregularities that change rapidly compared to the synthetic aperture (the synthetic aperture length of Biomass projected at the ionospheric height is about 20 km), inducing defocusing (seen as a loss of contrast) and intensity scintillation (patterns in the intensity images) that degrade the quality of the radiometric products. These distortions occur predominantly in the regions close to the geomagnetic equator [7] in the very early morning and evening times due to the characteristic appearance of instabilities of ionospheric plasma in these regions, as well as near the poles.

From the signal processing point of view, one can benefit from these adverse effects by retrieving information about the current state of the ionosphere while correcting the images. The ionospheric calibration of the images itself will allow the generation of 2-D TEC maps with the very high resolution that SAR provides. We will exploit the proportionality relationship between FR, phase advance, and TEC. Biomass will have a

Manuscript received 26 March 2024; revised 30 June 2024; accepted 2 August 2024. Date of publication 8 August 2024; date of current version 30 August 2024. This work was supported by the German Academic Exchange Service (DAAD) under Grant 57478193. *(Corresponding author: Felipe Betancourt-Payan.)*

The authors are with the Microwaves and Radar Institute, German Aerospace Center (DLR), 82234 Weßling, Germany (e-mail: felipe.betancourtpayan@dlr.de).

Digital Object Identifier 10.1109/TGRS.2024.3440628

Sun-synchronous polar low Earth orbit (average altitude of 660 km) with an orbital period of around 1.5 h. Beyond the calibration of the SAR images, the high-resolution TEC products over large areas unlock important scientific research opportunities, such as improving ionospheric equatorial irregularity models or the effect of space weather events in the polar regions.

There exist several calibration proposals for this challenging aspect of the mission. These exploit the FR [8], refocusing with an autofocus (AF) algorithm or a combination of both [9]. This article aims to characterize the residual errors expected after these calibration approaches. This article is structured as follows. Section II introduces the methodology and assumptions to solve this problem. We show that the error standard deviation can be expressed as the sum of different error sources. Section III discusses the residual errors after a multisquinted version of the Bickel and Bates algorithm for the estimation of FR; it also analyzes the impact of geomagnetic field uncertainty in TEC retrieval when using the FR. Section IV analyzes the remaining errors for a phase-based estimation with an AF. Section V discusses and compares the suitability of the two methods, and Section VI concludes this article with a summary.

II. Problem Statement

The propagation of radar waves through the ionosphere results in a perturbation of the amplitude, phase, and polarization of the signals [10]. We will use in our analysis the two following assumptions: 1) the perturbations show a specific consistency when observed from different positions along the satellite track, which allows us to model the impact as coming from a single surface (not necessarily spherical or ellipsoidal) and 2) the perturbations at spatial scales larger than the extension of the projection of the radar beam on the ionospheric surface have been successfully calibrated at previous processing stages. The former assumption is frequently found in the literature and justified by the continuity in the models of the ionospheric height [11], as well as supported by data collected from previous missions [12]. The latter assumption is justified by the dense sampling used in SAR, which allows the estimation of large-scale perturbations with large averaging windows. Following the previous discussion, we can approximate the impact on the radar waves by using a turbulent, stationary, dispersive, Doppler-dependent, and elevation-dependent perturbation field. The field consists of irregularities in the electron density, which directly translate into a phase and polarization distortion of the signals [13]. The spatial statistics of the stationary phase distortion field are often described by the Rino power law expression [14],

$$\Phi_\phi(\kappa_x,\kappa_y) = \frac{\lambda^2 \cdot r_e^2 \cdot \sec^2\theta_{\text{inc}} \cdot ab \cdot (2\cdot\pi/1000)^{p+1} \cdot C_k L}{\left(\kappa_0^2 + A\cdot\kappa_x^2 + B\cdot\kappa_x\cdot\kappa_y + C\cdot\kappa_y^2\right)^{(p+1)/2}} \tag{1}$$

where ϕ refers to the phase advance, κ_x and κ_y describe the orthogonal spatial frequencies in the reference geometry of the ionosphere, in this case, the geomagnetic North and East directions, λ is the carrier wavelength, r_e is the classical electron radius, θ_{inc} is the incident angle onto the ionospheric surface, p is the ionospheric spectral index, $C_k L$ is the vertically integrated strength of turbulence at 1-km scale, and $\kappa_o = 2\pi/l_o$ is the outer scale wavenumber. The A, B, and C parameters relate the magnetic field and anisotropy factors to the direction of propagation of the radar waves [15]. The relationship between the two-way phase advance ϕ, TEC, and FR Ω can be expressed as

TABLE I

Parameters Used for the Ionospheric Realization

Location Polar ROI (lat, lon)	(65.5, 11.0) [deg, deg]
$C_k L$	10^{32}
Outer scale l_0	20 km
Anisotropy $a:b$	5:1
Spectral index p	2.65
Ionospheric height h_{iono}	351 km

$$\phi = \frac{\zeta\cdot 4\cdot\pi}{c_0\cdot f}\cdot \text{TEC} \tag{2}$$

and

$$\Omega = \zeta\cdot\frac{q_e\cdot\vec{B}\cdot\hat{k}}{c_0\cdot m_e\cdot f^2}\cdot\text{TEC} \tag{3}$$

where $\zeta \approx 40.31\, m^3/s^2$ is a constant, c_0 is the velocity of propagation in vacuum, f is the frequency, q_e is the electron charge, $\vec{B}$ is the Earth's electromagnetic field vector, $\hat{k}$ is the direction of propagation of the radar waves in the same reference frame, and m_e is the electron mass. The power spectral density (PSD) of the FR can be related to (1) as follows:

$$\Phi_\Omega(\kappa_x,\kappa_y) = \left(\frac{q_e\cdot\vec{B}\cdot\hat{k}}{m_e\cdot f\cdot 4\cdot\pi}\right)^2\cdot\Phi_\phi(\kappa_x,\kappa_y). \tag{4}$$

The statistical characterization of the errors in estimating the turbulent component of the ionosphere will result from filtering these PSD functions with the frequency response of the calibration algorithms. For this approach to yield representative results for a SAR acquisition, we need to make the additional assumption that this PSD is known (e.g., via models such as wideband model (WBMOD) for ionospheric scintillation [16]) or can be estimated from the data. The direct estimation from the data can be carried out by fitting the PSD of the observed ionosphere to the parameters of (1) or an approximation of it. For example, in [17], where the fitting is done based on what is retrieved in the interferometric correction, or [18], where the equatorial scintillation stripe signature is used. However, the correctness of the methodology and the illustrative power of the presented results are not affected.

For example, Fig. 1 shows one ionospheric realization in the Biomass observation geometry (satellite flying along the horizontal axis) according to the model described above for a region close to the North pole. The parameters of the simulation are listed in Table I. The Biomass End-to-End Performance Simulator (BEEPS) [19] is used to incorporate the ionospheric perturbations (phase and change in polarization) in the simulated SAR raw data.

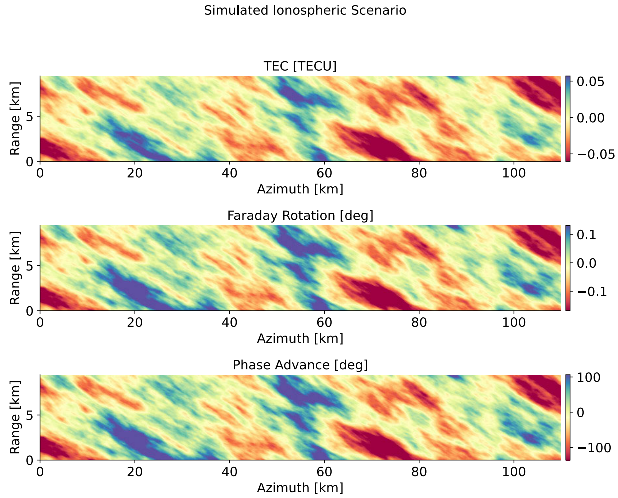

Fig. 1. Ionospheric irregularity realization generated with the parameters in Table I. From the TEC map (top), FR (middle) and phase (bottom) maps are obtained from (2) and (3).

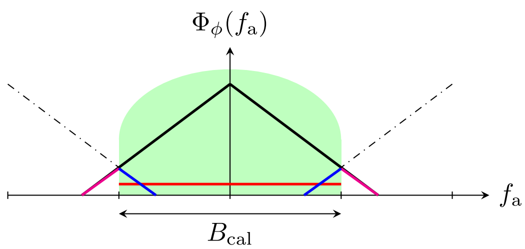

Fig. 2. Sketch of the PSD of the phase advance error observed by the SAR (black). The green area describes the calibration filter used in the ionospheric mitigation algorithms also used for ionospheric imaging. The blue, magenta, and red lines correspond to the intrinsic filtering errors caused by aliasing, limited bandwidth, and thermal noise, respectively. Aliasing replicas (dashed lines) occur by sampling the nonbandlimited ionospheric irregularity (here described by a power-law) function.

Fig. 2 sketches the errors (in blue, red, and magenta) in the ionospheric signal when reconstructing the phase field from the data. For simplicity, Fig. 2 refers to the azimuth dimension of the survey (f_a refers to azimuth or Doppler frequency), but the situation in the range is analogous. The green area corresponds to the filter that defines the calibration operations and extends to what we define as calibration bandwidth, B_{cal}. The blue lines within the filter correspond to the aliased power coming from the tails of the first spectral replicas. Replicas occur because of the sampling of a nonbandlimited field. The magenta solid lines outside the filter correspond to the power outside the calibration bandwidth, whereas the red line represents the power of thermal noise.

The one-sided PSD of the error when reconstructing the irregularity field (in our case, either using the FR or the phase signature that it leaves in the image) can be approximated as the sum of the contributions within and outside the calibration bandwidth, $f_a \leq B_{cal}/2$ and $f_a > B_{cal}/2$, respectively, as described in (5), as shown at the bottom of the next page. $\Phi_N(f_a)$ is the PSD of the thermal noise, assumed constant for white noise. The variance of the phase error (or the FR) is given in (6), as shown at the bottom of the next page: the first integral corresponds to the error within the band, composed by the noise plus the tails of the aliased replicas (that as we will see, might or might not be neglected). Here, i is the index of the aliasing replicas that occur every sampling

TABLE II

SIMULATION PARAMETERS

Satellite altitude h_{sat}	660 km
Incidence angle θ_{inc}	25 deg
Antenna diameter	12 m
Carrier frequency f_0	435 MHz
Pulse Repetition Frequency (PRF)	1475.506 Hz
Azimuth Bandwidth (B_a)	1229.588 Hz
Range Sampling Frequency (RSF)	7565217.4 Hz
Range bandwidth (B_r)	6877470.363 Hz

frequency f_{samp}. The calibration filter B modulates these two components. The second integral shows the high frequency of the original perturbation lost because it falls outside the calibration window.

For the characterization of the errors, i.e., the residual disturbances in the imaging of the ionospheric irregularities, we will consider the two ionospheric calibration algorithms available in the Biomass Ground Processor Prototype (GPP) [20]. They should provide exemplary ionospheric recovery maps and the residual errors expected in Biomass images. The baseline for ionospheric correction in Biomass uses the estimation of the FR using the Bickel and Bates algorithm [8]. The estimation of the FR has proven to be a robust and effective method for ionospheric imaging in quad-pol systems. Still, the accuracy of the Bickel and Bates algorithm is latitude and signal-to-noise ratio (SNR)-dependent. From (3), one can see that the sensitivity depends on the value of the dot product $\vec{B} \cdot \hat{k}$. Close to the geomagnetic equator, these two vectors are almost perpendicular, which makes FR-based calibration algorithms insensitive to the ionosphere. Fig. 3 shows a global map of the error in the TEC estimation for a 1° error in the FR measurement. The geographic variations come from the geomagnetic field distribution. Note that from (3), errors in the FR scale to errors in TEC with the inverse of $\vec{B} \cdot \hat{k}$, and since at low latitudes the dot product is very small in practice it not possible carry out ionospheric inversion at the so-called *equatorial gap*. This region is depicted in red in Fig. 3.

For tracking fast ionospheric variations within the synthetic aperture, which might degrade the performance of the FR estimation, the GPP also incorporates a map-drift autofocus (MDA) algorithm [9], [21], [22]. This method takes observations of local defocusing across the image and transforms them into second derivatives of the phase variation along azimuth, which can also be integrated into TEC estimates. The AF performance depends on the image contrast and content, where a lack of contrast significantly reduces its robustness (and attractiveness); therefore, the MDA is kept as a backup solution in the processing flow. The fact that the MDA reconstructs higher order errors from second derivative measurements makes it insensitive to zeroth- and first-order errors (this is the reason for the previous assumption that any slowly varying background component is assumed to be removed). Errors in the measurements integrate into random walks during the double integration step. Sections III and IV will present the error characterization for the two suggested algorithms. Table II summarizes the main parameters for the simulations on the L-band image in Fig. 4 (in the absence of satellite P-band data, we used an actual ALOS-2 image).

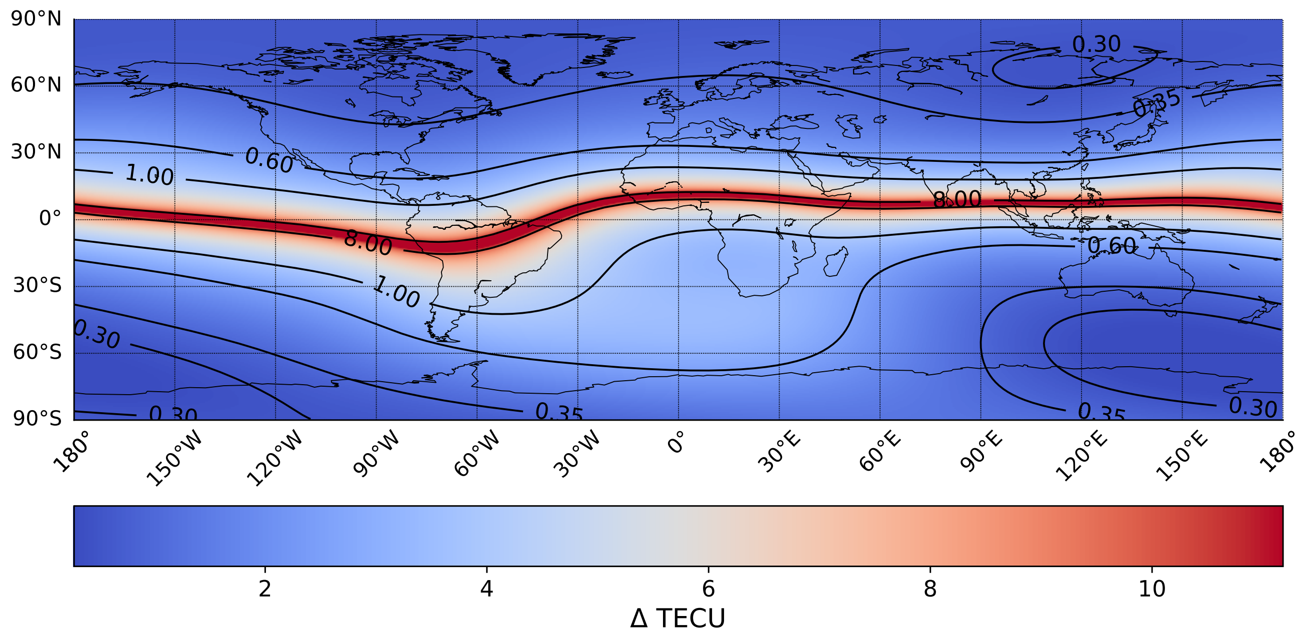

Fig. 3. Error in TEC estimation for 1° error in the FR measurement. The geometry is an ascending polar orbit with a 25° incidence angle onto the horizontal ionospheric layer. The red area shows the equatorial gap, where $\vec{B} \cdot \hat{k}$ tends to zero and there is no FR sensitivity.

For this article, we ingested the reflectivity image into the BEEPS/GPP processing chain to investigate the ionospheric effects and realistically process the data, demonstrating the capability of the MDA in a realistic scenario.

III. Bickel and Bates-Based Estimation

The examples in this section will be generated using a multi-squinted version, based on azimuth sublooks, of the Bickel and Bates estimator to estimate the FR. For a detailed description of the fundamentals, the reader should refer to [8], [23], and [24]. The calibration bandwidth is estimated from the PSD of the data. Fig. 5 shows that the azimuth cutoff frequency (gray) can be chosen where the PSD of the simulated FR field in the middle of Fig. 1 (blue) cuts the noise floor of the simulation (red). The noise floor depends on the SNR and the polarimetric coherence as discussed in [8] and [25]. The polarimetric coherence is related to the SNR as follows:

$$\gamma_{\mathrm{SNR}} = \frac{\mathrm{SNR}}{1+\mathrm{SNR}}. \tag{7}$$

The variance of the additive noise to FR (depicted with the red dashed line in Fig. 5) is given by (8), as shown at the bottom of page 6, where Li_2 is the Euler dilogarithm. An SNR of 25 dB leads to 0.996484 polarimetric coherence, and the corresponding filter azimuth bandwidth allows 476 nonoverlapping sublooks to cover the entire SAR azimuth bandwidth in the multisquint processing.

The calibration filter can be extended to the range dimension to improve noise suppression. For this analysis, we give it a rectangular shape in range, with a cutoff frequency that limits the noise inside the calibration bandwidth. Similar to (6), the final expression for the error variance is given in (9), as shown at the bottom of page 6. Here, B represents the spectral shape of the averaging window, S_{cbw} is the area of the calibration bandwidth, and S^c_{cbw} is its complement. $\mathrm{d}f_r$ is the frequency in the slant range direction, and i and k are the indexes of the replicas both in azimuth and range. Note that $i, k \in \mathbb{Z} \setminus \{0\}$. In the following, we only consider 2-D rectangular bandpass filters, but we can also use more elaborate filters oriented along the geomagnetic field for better performance.

$$\Phi_{\Delta\phi}(f_{\mathrm{a}}) = \begin{cases} \Phi_\phi(f_{\mathrm{a}}) & \text{for } f_{\mathrm{a}} > B_{\mathrm{cal}}/2 \\ B \cdot \left(\Phi_{\mathrm{N}}(f_{\mathrm{a}}) + \sum_{i=1}^{+\infty} \left(\Phi_\phi\left(f_{\mathrm{a}} + i \cdot f_{\mathrm{samp}}\right) + \Phi_\phi\left(f_{\mathrm{a}} - i \cdot f_{\mathrm{samp}}\right)\right)\right) & \text{for } f_{\mathrm{a}} \le B_{\mathrm{cal}}/2 \end{cases} \tag{5}$$

$$\sigma^2_{\Delta\phi} = 2 \cdot \left(\overbrace{\int_0^{B_{\mathrm{cal}}/2} \underbrace{B}_{\text{cal. filter}} \cdot \left(\underbrace{\Phi_{\mathrm{N}}(f_{\mathrm{a}})}_{\text{noise}} + \underbrace{\sum_{i=1}^{+\infty} \left(\Phi_\phi\left(f_{\mathrm{a}} + i \cdot f_{\mathrm{samp}}\right) + \Phi_\phi\left(f_{\mathrm{a}} - i \cdot f_{\mathrm{samp}}\right)\right)}_{\text{aliasing}} \right) \mathrm{d}f_{\mathrm{a}}}^{\text{inside of band}} + \overbrace{\int_{B_{\mathrm{cal}}/2}^{\infty} \Phi_\phi(f_{\mathrm{a}})\, \mathrm{d}f_{\mathrm{a}}}^{\text{outside of band}} \right). \tag{6}$$

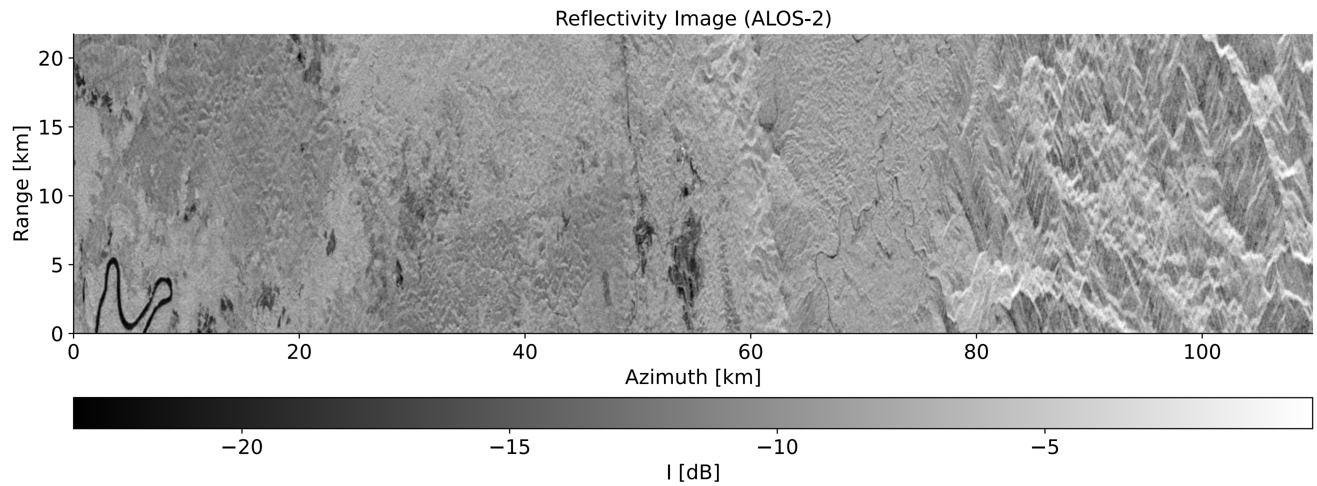

Fig. 4. Reflectivity image used in the simulations. The scene shows a forested and mountainous area with the L-band sensor ALOS-2 over Indonesia. An L-band acquisition is used in the absence of spaceborne P-band data.

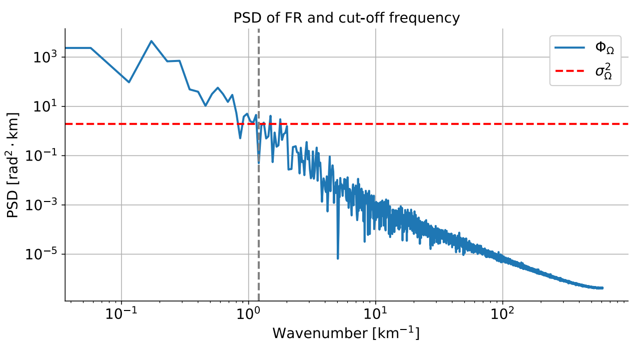

Fig. 5. Azimuth profile PSD of the simulated phase scaled to FR. The red horizontal line represents the noise power corresponding to the simulated with an SNR $= 25$ dB and $\gamma = 0.996484$. The vertical dashed line represents half the bandwidth of one of the 476 sublooks used in this simulation.

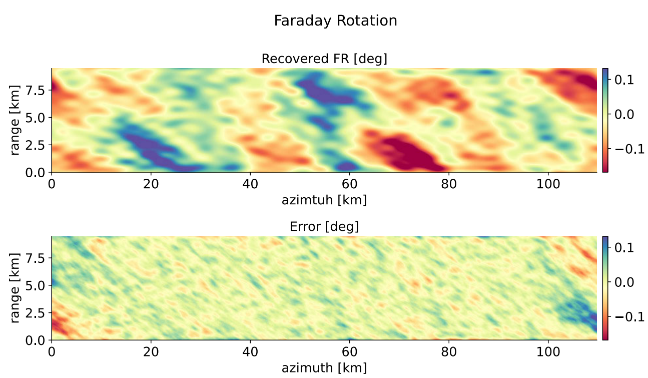

Fig. 6. (Top) Recovered FR map using Bickel and Bates and (bottom) corresponding error map for the simulated FR field in Fig. 1.

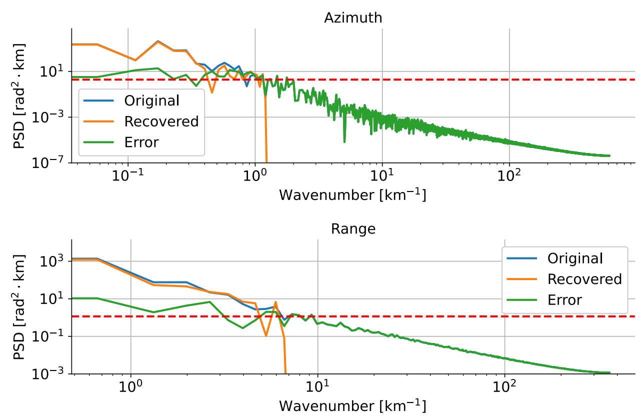

Fig. 7. (Top) Azimuth and (bottom) range PSD of the simulated FR field (blue), the recovered FR field using the multisquint approach (orange), and errors (green). Note that the frequency coverage of the recovered FR field only extends to the cutoff frequencies.

Fig. 6 shows the FR map recovered with this technique. Note the agreement in the structure with respect to the middle map in Fig. 1 and range of values (with a slight variability). Any discrepancy is better visualized in the error map below. This error contains mainly the high-frequency component of the original field that is not seen by the calibration bandwidth (note that the small structure still preserves the orientation). We can better validate this claim by looking at Fig. 7, where we compare the PSD of the recovered FR field (orange) to the PSD of the original one (blue). For reference, the PSD of the error is shown in green. Here, one can see that, as expected, the frequency coverage of the recovered FR only extends to the cutoff frequency, so the error outside of the band is just the part of the spectrum not seen by it. Inside the band, there is a part of the noise spectrum and a smaller contribution coming from possible interpolation errors in the processing. Note that this error is still more than two orders of magnitude smaller than the original signal. The aliasing contribution depends on the sampling and the transfer function of the calibration filter, which, for the FR, is narrow compared to the high SAR sampling, making it negligible.

Fig. 8 shows the apparent azimuth and range resolution corresponding to the simulated ionospheric scenario for different SNRs. Here, a Monte Carlo simulation was carried out, generating various additive noise realizations for the FR field and choosing the cutoff frequency by looking at the magnitude of the corresponding Wiener filter (maintaining only the part before its magnitude reached -3 dB). The noise floor decreases for higher SNR, and a larger apparent bandwidth can improve the resolution to the kilometer scale in azimuth and subkilometer scale in range. Because the irregularity field is described as stationary, the variance of the error field is also stationary, and it is reasonable to characterize it with the standard deviation, $\sigma_{\Delta\Omega}$. Disregarding aliasing and interpolation errors, Fig. 9 shows the change in FR standard deviation for different SNRs. According to this, the main

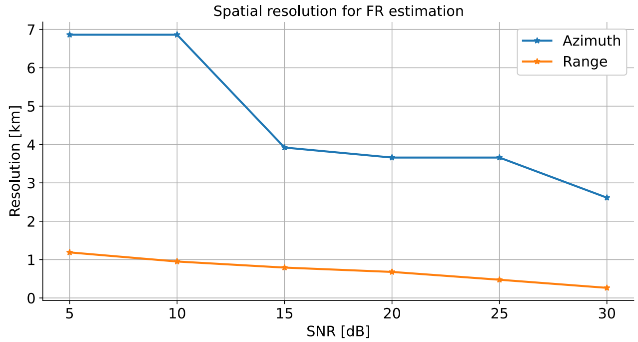

Fig. 8. For the simulated scenario, the resolutions in range and azimuth of the retrieved FR with the multisquint approach for different SNRs after a Monte Carlo simulation. The cutoff frequencies in range and azimuth correspond to the first −3-dB cut of the corresponding Wiener filter.

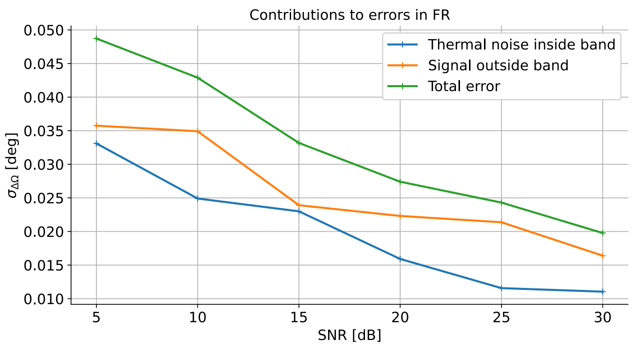

Fig. 9. Standard deviation of different error components (thermal noise inside of the band and signal outside) and the sum. Note that the main contribution comes from the signal part, which is not seen by the calibration bandwidth.

contribution to the error comes from the part of the spectrum that falls outside of the calibration bandwidth.

As described in [8], the estimated FR can be scaled to phase and used to correct phase errors. We can assess the impact of the residual errors in the quality of the image by looking at the radiometry. With remaining phase errors after the calibration, apart from the defocusing, the interpretation of the images will be distorted by discrepancies in the radiometry. We refer to the change power Δ_{P} with respect to the image without any distortion $|A|$ over an averaging window, i.e.,

$$\Delta_{\mathrm{P}} = \frac{\mathbb{E}\left[|A'|^2\right]}{\mathbb{E}\left[|A|^2\right]} \tag{10}$$

where $|A'|$ is the amplitude of the image with the residual errors after calibration. Errors in the radiometry distort the measured radar cross section of the imaged targets and mislead the interpretation of the data. Fig. 10 shows the radiometric error after the FR scaled to dB. The FR-based approach gives a good result in a polar scenario with a standard deviation of ≈0.068 dB.

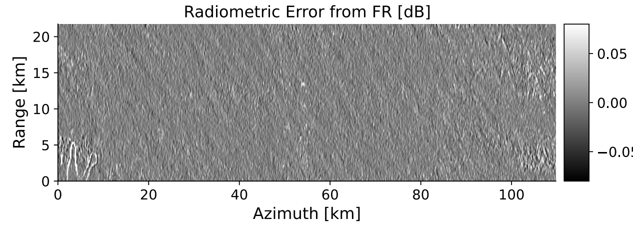

Fig. 10. Radiometric error after correction based on the FR field recovered in Fig. 6 scaled to phase.

A. Global Uncertainty Due To Geomagnetic Field

In addition to the calibration residuals presented so far, other error sources come from system uncertainties or model variability. We shall consider geometry errors that affect the line-of-sight (LOS), uncertainties introduced by the thin layer approximation and ionospheric height estimation, and residuals in the antenna pattern compensation, which are seen as polarimetric crosstalk contaminating the FR estimation, to mention a few. Assuming that these variables are controlled to a certain extent, we will shortly comment on the effect of the geomagnetic field uncertainty.

From [26], average values for the geomagnetic field vector uncertainty $\vec{\sigma}_B$ associated with the International Geomagnetic Reference Field (IGRF) model are 144 nT for the North (X), 136 nT for the East (Y), and 293 nT for Down (Z) components. The geomagnetic field vector, together with the LOS, is used for converting from FR into TEC and phase advance; as we will see in the following, this uncertainty introduces nonnegligible errors in the ionospheric retrieval with the Biomass system. Following the error propagation method described in [27] and assuming that the single uncertainties are independent and the orbit is polar, the uncertainty in $\vec{B}\cdot\hat{k}$ is given by (11), as shown at the bottom of the next page, which simplifies to

$$\sigma_{\vec{B}\cdot\hat{k}} = \sqrt{\hat{k}^2 \cdot \vec{\sigma}_B^{\,2}}. \tag{12}$$

Considering that Biomass has a polar orbit with a left-looking geometry and a mean incidence angle onto the ionospheric horizontal plane of 25°, this uncertainty is 271.70 nT, constant everywhere on Earth. Different values are obtained with orbit inclinations or incidence angles, reflected in $\hat{k}$. Similarly, when estimating TEC (background or turbulent component) from FR, the uncertainty $\sigma_{\mathrm{TEC}}(\Omega)$ depends on $\sigma_{\vec{B}\cdot\hat{k}}$ and the local $\vec{B}\cdot\hat{k}$

$$\sigma_{\mathrm{TEC}}(\Omega) = \sqrt{\left(\frac{\partial \mathrm{TEC}}{\partial\left(\vec{B}\cdot\hat{k}\right)}\right)^2 \cdot \sigma_{\vec{B}\cdot\hat{k}}^2} \tag{13}$$

$$\sigma_\Omega^2 = \frac{1}{16}\left(\frac{\pi^2}{3} - \pi\cdot\sin^{-1}\gamma_{\mathrm{SNR}} + \left(\sin^{-1}\gamma_{\mathrm{SNR}}\right)^2 - \frac{\mathrm{Li}_2\left(\gamma_{\mathrm{SNR}}^2\right)}{2}\right) \tag{8}$$

$$\sigma_{\Delta\Omega}^2 = \overbrace{\int\int_{S_{\mathrm{cbw}}} B\cdot\left(\Phi_{\mathrm{N}} + \sum_{i=-\infty}^{+\infty}\sum_{k=-\infty}^{\infty}\Phi_\Omega[i,k]\right)\mathrm{d}f_r\,\mathrm{d}f_{\mathrm{a}}}^{\text{inside of band}} + \overbrace{\int\int_{S_{\mathrm{cbw}}^c}\Phi_\Omega\,\mathrm{d}f_r\,\mathrm{d}f_{\mathrm{a}}}^{\text{outside of band}} \tag{9}$$

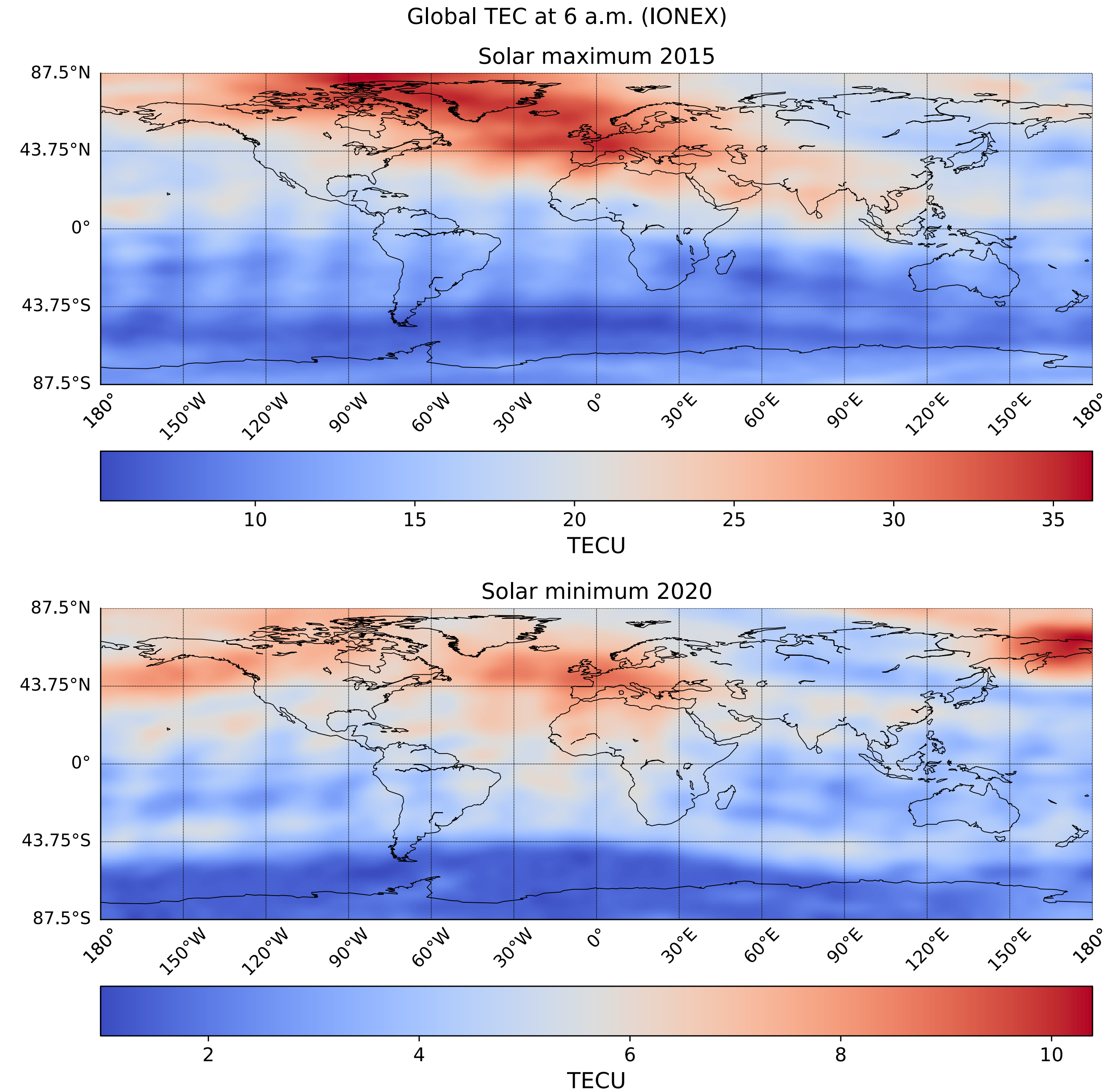

Fig. 11. Global TEC maps at 6 A.M. extracted from IONEX database for the 40th DoY 2015 (solar maximum, top) and 2020 (solar minimum, bottom).

with

$$\frac{\partial \mathrm{TEC}}{\partial\left(\vec{B}\cdot\hat{k}\right)} = -\frac{c_0 \cdot m_e \cdot f^2}{\zeta \cdot q_e} \cdot \frac{1}{\left(\vec{B}\cdot\hat{k}\right)^2} \cdot \Omega(\mathrm{TEC}). \tag{14}$$

Note that in (14), we highlight that the uncertainty in TEC depends on the local FR angle that is given by the value of TEC itself. Plugging $\Omega(\mathrm{TEC})$ from (3), we come to the following expression for the uncertainty in TEC based on the local TEC and $\vec{B}\cdot\hat{k}$:

$$\sigma_{\mathrm{TEC}}(\mathrm{TEC}) = \frac{\mathrm{TEC}}{|\vec{B}\cdot\hat{k}|} \cdot \sigma_{\vec{B}\cdot\hat{k}}. \tag{15}$$

Now, we proceed to give some representative numbers. For that, Fig. 11 shows the global TEC maps from the ionosphere map exchange (IONEX) database [28] at 6 A.M. that corresponds to what Biomass will observe (with the Sun-synchronous orbit, the same can be done for 6 P.M.), and

$$\sigma_{\vec{B}\cdot\hat{k}} = \sqrt{\left(\frac{\partial \vec{B}\cdot\hat{k}}{\partial B_X}\right)^2 \cdot \sigma_{B_X}^2 + \left(\frac{\partial \vec{B}\cdot\hat{k}}{\partial B_Y}\right)^2 \cdot \sigma_{B_Y}^2 + \left(\frac{\partial \vec{B}\cdot\hat{k}}{\partial B_Z}\right)^2 \cdot \sigma_{B_Z}^2} \tag{11}$$

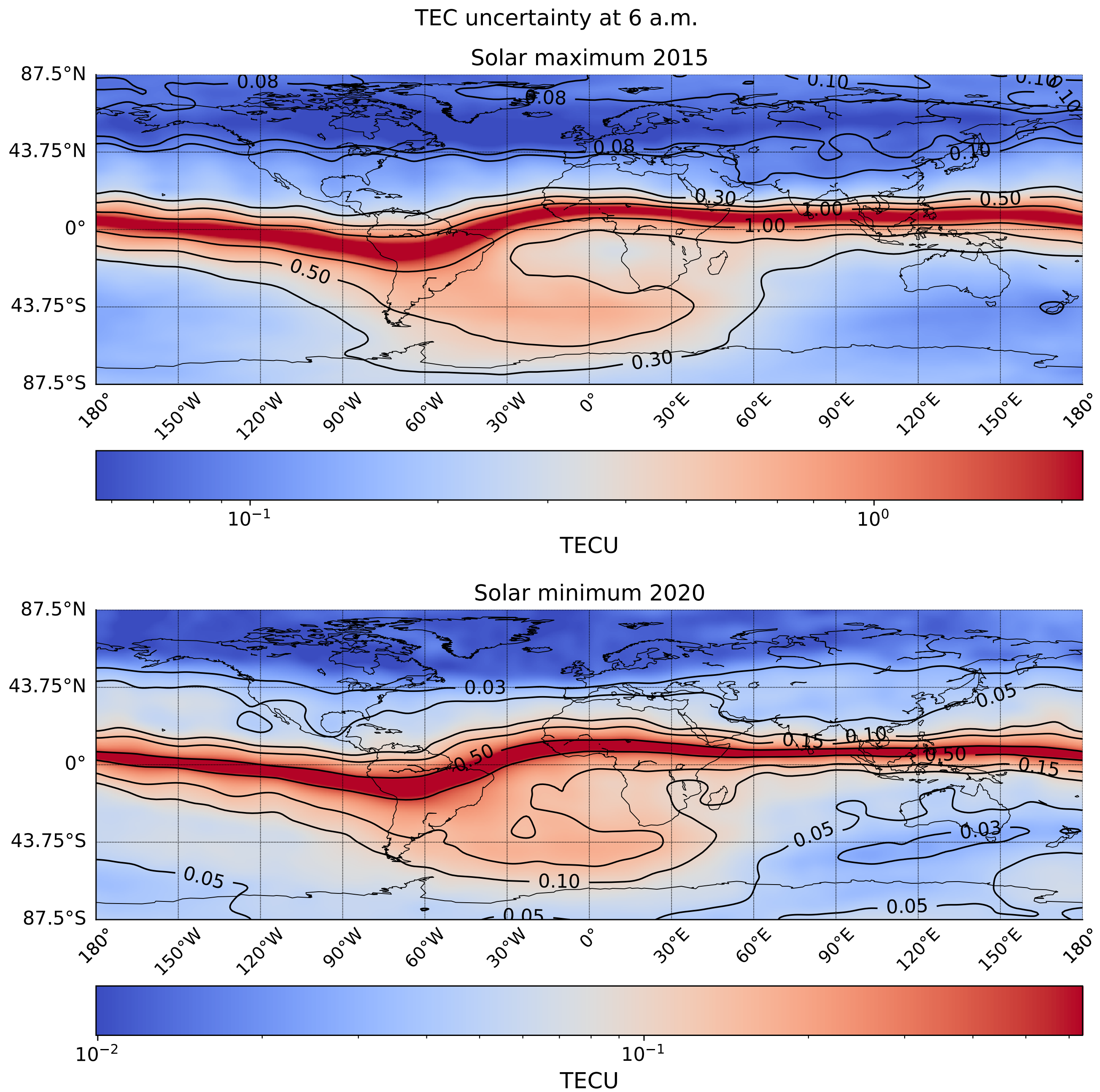

Fig. 12. Global uncertainty in estimating the background TEC from FR. Consider the ascending node of a polar Sun-synchronous orbit with the Biomass left-looking geometry at a time of solar maximum (top) and solar minimum (bottom).

we do this for two dates: the 40th day of the year (DoY) 2015 (solar maximum) and 2020 (solar minimum). The color bars show that in the solar maximum times, the TEC values triple the solar minimum values. Note that the irregularities in the map potentially come from the interpolations over the low resolution of the IONEX products; however, it does not invalidate our analysis since the purpose of this article is to have a sense of the global sensitivity variation. Putting these values in (15) with the local $\vec{B}\cdot\hat{k}$ leads to Fig. 12. Here, we see the uncertainty in TEC estimation from FR for the Biomass geometric configuration at a time of solar maximum and a time of solar minimum. Note that the uncertainty distribution strongly depends on the geomagnetic field dipole and its anomalies and that the higher uncertainty is found around the geomagnetic equator.

IV. Map-Drift Autofocus

An essential factor to consider when assessing the performance of the MDA is that it works with partially overlapped blocks across the image. Because of this, the measurements constitute a map of second derivatives (of the variation of the phase in the azimuth direction) that represents the difference between the average slopes across the two corresponding nonoverlapping synthetic aperture sublooks. In Fig. 13, they are illustrated by the two slopes in red and green in the sublooks shaded in yellow and orange. Because of the block operation and the assumption that the second derivative is constant across the block, some averaging happens in range and azimuth, too. Note that the second derivative map is subsampled to the block center spacing in both directions, leading to significant aliasing in the solution, as we will see.

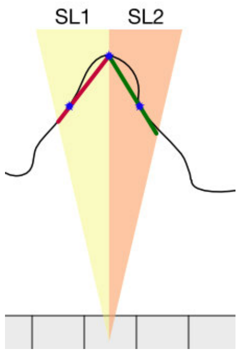

Fig. 13. Second derivative of azimuth variation across the synthetic aperture as seen by splitting the azimuth spectrum in the MDA.

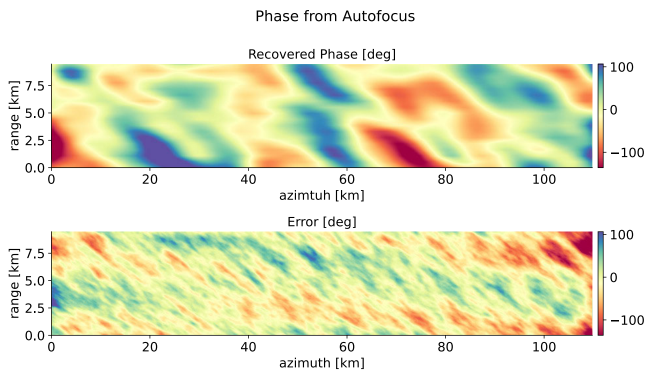

Fig. 14. (Top) Recovered phase after applying MDA and (bottom) corresponding error map.

The integration of this second derivative map into a TEC map can be done, for example, with a Wiener filter [9] or with a weighted least-squares (WLS) approach [21]. Either method will minimize the effect of the integrated random walks that derive from integrating errors in the second-derivative measurement. Even though random walks fail to be stationary, complicating the spectral analysis, an iterative MDA with a WLS integration has shown to dampen them to a reasonable extent. The MDA is an iterative method, and in each iteration, a phase map of the original size is obtained using a linear interpolation.

Fig. 14 shows the phase field recovered by the MDA with a WLS integration. In this simulation, we use a 128×128 pixel window (644×1106 m in azimuth and range) with shifts of 40 and 64 pixels in azimuth and range. Compared to the simulated field in Fig. 1, the MDA outputs a smoothed solution due to the averaging of the second derivative across the synthetic aperture, block averaging, aliasing due to sampling, integration, and linear interpolation reconstruction. Similar to the previous case, the error map presents structures aligned with the simulated field, but not only is the high-frequency component appreciated, as in the last case. This is better seen in the PSD azimuth profiles shown in Fig. 15: the PSD of the recovered phase field (orange) extends to the

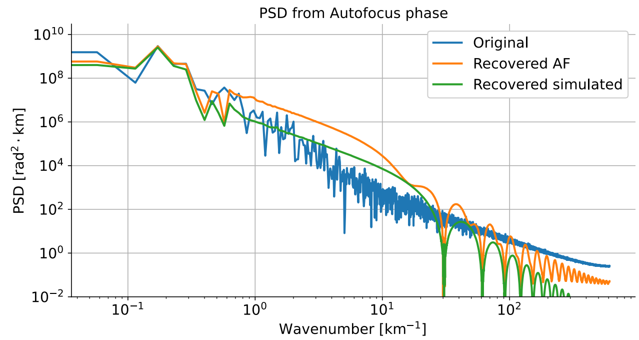

Fig. 15. Azimuth profile of the PSD of the simulated phase map (blue), the recovered after MDA (orange), and the result of applying the equivalent transfer functions to the simulated PSD (green).

TABLE III
PARAMETERS USED FOR EQUATORIAL SIMULATION

Location Equator ROI (lat, lon)	(19.0, 9.5) [deg, deg]
$C_k L$	10^{32}
Outer scale l_0	20 km
Anisotropy $a : b$	2:1
Spectral index p	2.65
Ionospheric height h_{iono}	351 km

end of the frequency coverage. This can be shown to be an effect of the corresponding aliasing (also responsible for the higher energy at the beginning of the PSD) and modulation of the frequency response of the MDA operations (green) as described in (16), as shown at the bottom of the page. Here, L is the frequency response of the linear interpolation operation (a sinc^2), $j \cdot \omega_1$ represents the differentiation in the frequency domain, $\frac{1}{j \cdot \omega_2}$ is the integration, M represents the block averaging, and again the summations with $i, k \in \mathbb{Z} \setminus \{0\}$ correspond to the aliasing that now plays a role because of the much lower sampling rate. Note that ω_1 and ω_2 are different since one represents the derivative with a step corresponding to two sublook centers, and the other corresponds to the displacement of the block centers in azimuth. The development of random walks has not been included in (16), but the results shown in Fig. 15 are still consistent. This shows that the iterative WLS integrator can cancel them appropriately.

As in Section III, we also use the residual radiometric error to assess the calibration performance (see Fig. 16). As shown in Fig. 14, the error map has larger granularity, also seen in the radiometric error map. In this case, the AF performs worse than the FR-based approach with radiometric errors with a standard deviation of 0.107 dB.

V. CONVENIENCE OF DIFFERENT CALIBRATION ALGORITHMS

So far, we have discussed a method for characterizing errors in two calibration approaches. Now, it is interesting to discuss their suitability in the ionospheric correction and imaging process. Regarding the Bickel and Bates measurement, for

$$\Phi_{\phi,\text{AF}} = \overbrace{L^2}^{\text{interpolation}} \cdot \overbrace{\frac{1}{(j \cdot \omega_2)^4}}^{\text{integration}} \overbrace{\left(\sum_{i=-\infty}^{\infty} \sum_{k=-\infty}^{\infty} \left(\underbrace{M^2}_{\text{averaging}} \cdot \underbrace{(j \cdot \omega_1)^4 \Phi_\phi[i,k]}_{\text{differentiation}} \right) \right)}^{\text{sampling}} \qquad (16)$$

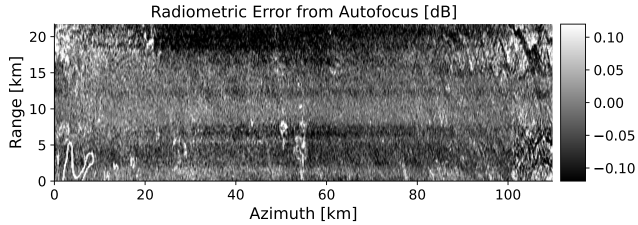

Fig. 16. Radiometric error after correction based on the phase field recovered in Fig. 14.

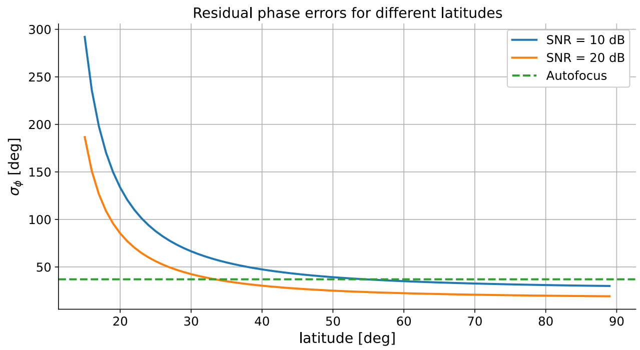

Fig. 17. Comparison of the expected performance estimating the phase screen in Fig. 1 using the FR and AF for two different SNRs and different latitudes along the prime meridian. The curves represent the FR performance that will change with latitude due to the variation in the $\vec{B} \cdot \hat{k}$ and SNR. The green horizontal dashed line shows the performance of the AF on the image in Fig. 4.

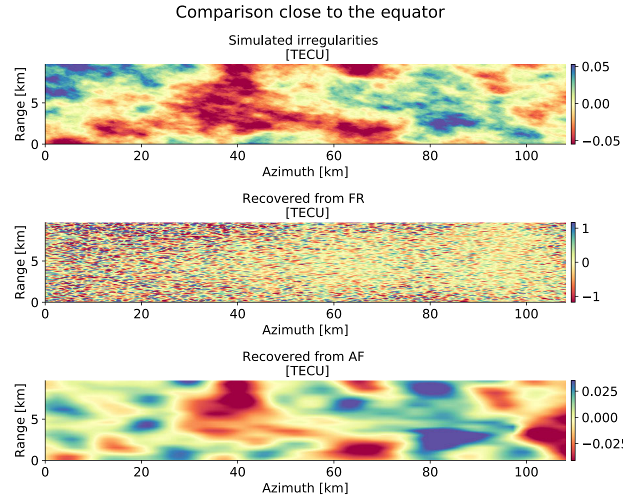

Fig. 18. Recovery of ionospheric irregularity maps closer to the equator. TEC map (top), recovered from FR (middle) and AF (bottom).

a fixed spectral index, the performance will be defined by $\vec{B} \cdot \hat{k}$, $C_k L$, the outer scale, and the noise floor, which will move up or down depending on the SNR, thus increasing or decreasing the cutoff frequency (Fig. 5). Conversely, for a fixed SNR, the cutoff frequency will also be determined by the PSD of the signal that would move up and down with $C_k L$ and $\vec{B} \cdot \hat{k}$, worsening the performance of this approach for smaller irregularity strength and when the FR sensitivity decreases compared to the SNR (toward the equatorial gap). Irregularities with larger outer scales focus the bigger portion of their energy in the low frequencies, so they can be resolved in higher SNR scenarios with a narrower filter. Due to the $\vec{B} \cdot \hat{k}$ latitude dependence, using the FR to correct for phase errors or directly measure TEC also leads to considerable errors due to the noise scaling toward the equator.

The performance of the phase estimation using the MDA is limited by the block sizes and overlapping factors (that define the new sampling grid and the aliasing introduced in the spectrum of the solution). The contrast and content of the image play an essential role in the accuracy of the estimation of the shift between sublooks, which, as discussed for the case of split-band interferometry [29], is better estimated with larger block sizes at the expense of a loss in resolution due to block averaging. In addition, the fact that the measurements are not of absolute phase but of a second derivative map that has to be integrated imposes that the performance of the MDA also depends on the capability of the integrator (e.g., the WLS discussed in this article) to disregard outliers and dampen random walks. The errors in the estimation of the second derivative cannot be globally characterized since they depend on the contrast and content of each block. Moreover, the statistics of the developed random walks cannot be described with notions of stationary fields.

To compare the performance of both methods, we focus on the phase screen recovery (take the scenario in Fig. 1 as an example). The errors in the estimation of the FR discussed in Section III (for the 10- and 20-dB SNR cases) are scaled to phase with the corresponding $\vec{B} \cdot \hat{k}$ for different latitudes along the prime meridian. The curves in Fig. 17 show the standard deviation of the residual phase error after scaling from FR. Note that the performance rapidly decreases toward the equator. The green dashed line shows the standard deviation of the residual phase after applying the AF algorithm on Fig. 4, which is not latitude-dependent. Below around 50° for an SNR $= 10$ dB and 30° for an SNR $= 20$ dB the AF is expected to perform better.

For example, Fig. 18 shows the result for the simulation parameters in Table III and moving the simulation closer to the equator. Here, the irregularities are more aligned to the azimuth direction, and the AF can still recover their structure, opposite to when the estimation is based on the FR. Based on the FR, applying any phase correction would not be possible in such a case, so image restoration is only possible with the AF.

VI. Conclusion

Low-frequency SARs offer an exceptional possibility to obtain ionospheric maps with spatial resolutions significantly better than other systems (such as GNSS receivers). As part of the ionospheric calibration, Biomass produces ionospheric irregularity maps with resolutions of hundreds of meters or a couple of kilometers, depending on the algorithm used and its sensitivity. In addition, these maps can be generated covering similar latitudes within less than two hours. Despite its limitations, due to its sensitivity, the ionospheric Biomass products are expected to reinforce current areas of research and work in synergy with any other ionospheric sensing approach. At this point, we highlight the importance of small-scale irregularity sensitivity, which poses a challenge in terms of calibration but is highly valuable for the scientific community.

In this study, we have provided an analytical description of the errors expected in Biomass ionospheric images. These were then compared to the results obtained using data simulated and processed with the Biomass simulator and prototype processors. We focused on two calibration approaches: one based on the estimation of the FR and one with an MDA. The errors from the FR approach come mainly from the high-frequency component of the ionospheric irregularities that are not captured by the calibration bandwidth. We demonstrated that the spatial resolution can be maintained to a few kilometers depending on the sensitivity. The errors from the MDA calibration approach, on the other hand, are mainly due to block averaging, sampling (which introduces aliasing in the frequency domain), and interpolation operations. We also addressed the issue with the random walks during the double integration and showed that they can be significantly reduced with a WLS integrator.

The scenario studied close to the pole shows a better performance of the FR than the MDA; however, one needs to account for the fact that good FR sensitivity is not always warranted. For this reason, the calibration of Biomass products shall be complemented by an AF algorithm when required. Sample cases arise when approaching the equatorial gap or when the strength of the irregularities is low compared to the SNR. The method described in this article can be extended to provide a global sensitivity analysis and characterization of Biomass ionospheric images, which will be the subject of subsequent research.

This article mainly focused on the filtering operations that make the calibration algorithms. In addition, one needs to account for error in other calibration steps (such as the antenna pattern compensation), and other system and model uncertainties. To complement this aspect, we carried out a sensitivity analysis when estimating the TEC from the FR based on the uncertainties in the geomagnetic field present in the IGRF. The uncertainty in the geomagnetic field vector introduces errors in the transformation from FR to TEC and phase, which are nonnegligible and the spatial structure of the uncertainly at a global scale depends on the Earth's magnetic field. The approach is based on error propagation with partial derivatives to analyze the contribution of each variable, and it can be extended to the rest of the variables in the system. This part of the discussion showed yet another factor to take into account when using the FR as a proxy for ionospheric estimation as its geographical limitations. Methods based on the phase error estimation have other difficulties but are not dependent on the $\vec{B} \cdot \hat{k}$ product. For this reason, we emphasize that both approaches should be complementary.

All this contributes to the understanding of error characteristics in terms of standard deviation and puts focus on the structure. This article is intended for the user to interpret different ionospheric calibrations and retrieval error sources. This knowledge will be relevant when using the provided ionospheric maps for applications such as ionospheric state characterization or scintillation model validation.

REFERENCES

[1] X. Pi, A. J. Mannucci, U. J. Lindqwister, and C. M. Ho, "Monitoring of global ionospheric irregularities using the worldwide GPS network," *Geophys. Res. Lett.*, vol. 24, no. 18, pp. 2283–2286, Sep. 1997, doi: 10.1029/97gl02273.

[2] C. T. Nguyen, S. T. Oluwadare, N. T. Le, M. Alizadeh, J. Wickert, and H. Schuh, "Spatial and temporal distributions of ionospheric irregularities derived from regional and global ROTI maps," *Remote Sens.*, vol. 14, no. 1, p. 10, Dec. 2021, doi: 10.3390/rs14010010.

[3] S. Basu, K. M. Groves, J. M. Quinn, and P. Doherty, "A comparison of TEC fluctuations and scintillations at ascension island," *J. Atmos. Solar-Terr. Phys.*, vol. 61, no. 16, pp. 1219–1226, Nov. 1999, doi: 10.1016/S1364-6826(99)00052-8.

[4] G. S. Bust and C. N. Mitchell, "History, current state, and future directions of ionospheric imaging," *Rev. Geophys.*, vol. 46, no. 1, pp. 1–23, Mar. 2008, doi: 10.1029/2006rg000212.

[5] ESA, "Report for mission selection: Biomass," European Space Agency (ESA), Noordwijk, The Netherlands, Tech. Rep. ESA SP-13214/1), Nov. 2012. [Online]. Available: https://earth.esa.int/eogateway/documents/20142/37627/BIOMASSReport-for-Mission-Selection-An-Earth-Explorer-to-observe-forestbiomass.pdf

[6] A. Moreira, P. Prats-Iraola, M. Younis, G. Krieger, I. Hajnsek, and K. P. Papathanassiou, "A tutorial on synthetic aperture radar," *IEEE Geosci. Remote Sens. Mag.*, vol. 1, no. 1, pp. 6–43, Mar. 2013, doi: 10.1109/MGRS.2013.2248301.

[7] L. Alfonsi et al., "Analysis of the regional ionosphere at low latitudes in support of the biomass ESA mission," *IEEE Trans. Geosci. Remote Sens.*, vol. 56, no. 11, pp. 6412–6424, Nov. 2018, doi: 10.1109/TGRS.2018.2838321.

[8] J. S. Kim, K. P. Papathanassiou, R. Scheiber, and S. Quegan, "Correcting distortion of polarimetric SAR data induced by ionospheric scintillation," *IEEE Trans. Geosci. Remote Sens.*, vol. 53, no. 12, pp. 6319–6335, Dec. 2015, doi: 10.1109/TGRS.2015.2431856.

[9] V. Gracheva, J. S. Kim, P. Prats-Iraola, R. Scheiber, and M. Rodriguez-Cassola, "Combined estimation of ionospheric effects in SAR images exploiting Faraday rotation and autofocus," *IEEE Geosci. Remote Sens. Lett.*, vol. 19, pp. 1–5, 2022, doi: 10.1109/LGRS.2021.3102597.

[10] M. I. Skolnik, "Introduction to radar," in *Radar Handbook*, vol. 2. New York, NY, USA: McGraw-Hill, 1962, p. 21.

[11] C. L. Rino, "On the application of phase screen models to the interpretation of ionospheric scintillation data," *Radio Sci.*, vol. 17, no. 4, pp. 855–867, Jul. 1982, doi: 10.1029/RS017i004p00855.

[12] G. Gomba, F. Rodríguez González, and F. De Zan, "Ionospheric phase screen compensation for the Sentinel-1 Tops and ALOS-2 ScanSAR modes," *IEEE Trans. Geosci. Remote Sens.*, vol. 55, no. 1, pp. 223–235, Jan. 2017, doi: 10.1109/TGRS.2016.2604461.

[13] C. L. Rino, "A power law phase screen model for ionospheric scintillation: 1. weak scatter," *Radio Sci.*, vol. 14, no. 6, pp. 1135–1145, Nov. 1979, doi: 10.1029/RS014i006p01135.

[14] C. S. Carrano, K. M. Groves, and R. G. Caton, "Simulating the impacts of ionospheric scintillation on l band SAR image formation," *Radio Sci.*, vol. 47, no. 4, pp. 1–14, Aug. 2012, doi: 10.1029/2011RS004956.

[15] C. Rino, *The Theory of Scintillation With Applications in Remote Sensing*. Hoboken, NJ, USA: Wiley, 2011, doi: 10.1002/9781118010211.

[16] J. A. Secan, R. M. Bussey, E. J. Fremouw, and S. Basu, "An improved model of equatorial scintillation," *Radio Sci.*, vol. 30, no. 3, pp. 607–617, May 1995, doi: 10.1029/94RS03172.

[17] G. Gomba and F. De Zan, "Bayesian data combination for the estimation of ionospheric effects in SAR interferograms," *IEEE Trans. Geosci. Remote Sens.*, vol. 55, no. 11, pp. 6582–6593, Nov. 2017.

[18] S. Ji, W. Chen, X. Ding, and C. Zhao, "Equatorial ionospheric zonal drift by monitoring local GPS reference networks," *J. Geophys. Res., Space Phys.*, vol. 116, no. A8, pp. 1–17, 2011, doi: 10.1029/2010JA015993.

[19] M. J. Sanjuan-Ferrer et al., "End-to-end performance simulator for the BIOMASS mission," in *Proc. 12th Eur. Conf. Synth. Aperture Radar (EUSAR)*, Jun. 2018, pp. 1–5. [Online]. Available: https://ieeexplore.ieee.org/abstract/document/8438196

[20] P. Prats-Iraola et al., "The BIOMASS ground processor prototype: An overview," in *Proc. 12th Eur. Conf. Synth. Aperture Radar (EUSAR)*, Jun. 2018, pp. 1–6. [Online]. Available: https://ieeexplore.ieee.org/document/8438145

[21] F. Betancourt-Payan, M. Rodriguez-Cassola, A. Benedikter, P. Prats-Iraola, and G. Krieger, "An autofocus algorithm for the recovery of ionospheric phase signatures in the biomass mission," in *Proc. 14th Eur. Conf. Synth. Aperture Radar (EUSAR)*, Jul. 2022, pp. 1–5. [Online]. Available: https://ieeexplore.ieee.org/document/9944332

[22] W. Carrara, R. Goodman, and R. Majewski, *Spotlight Synthetic Aperture Radar: Signal Processing Algorithms*. Norwood, MA, USA: Artech House, 1995. [Online]. Available: https://books.google.de/books?id=uztiQgAACAAJ

[23] S. H. Bickel and R. H. T. Bates, "Effects of magneto-ionic propagation on the polarization scattering matrix," *Proc. IEEE*, vol. 53, no. 8, pp. 1089–1091, Aug. 1965, doi: 10.1109/proc.1965.4097.

[24] A. Freeman, "Calibration of linearly polarized polarimetric SAR data subject to Faraday rotation," *IEEE Trans. Geosci. Remote Sens.*, vol. 42, no. 8, pp. 1617–1624, Aug. 2004, doi: 10.1109/TGRS.2004.830161.

[25] R. F. Hanssen, *Radar Interferometry: Data Interpretation and Error Analysis*, vol. 2. Cham, Switzerland: Springer, 2001, doi: 10.1007/0-306-47633-9.

[26] C. D. Beggan, "Evidence-based uncertainty estimates for the international geomagnetic reference field," *Earth, Planets Space*, vol. 74, no. 1, pp. 1–11, Dec. 2022, doi: 10.1186/s40623-022-01572-y.

[27] H. H. Ku, "Notes on the use of propagation of error formulas," *J. Res. Nat. Bur. Standards, Sect. C, Eng. Instrum.*, vol. 70C, no. 4, pp. 263–273, Oct. 1966, doi: 10.6028/jres.070c.025.

[28] S. Schaer, W. Gurtner, and J. Feltens, "IONEX: The ionosphere map exchange format version 1," in *Proc. IGS AC Workshop*, Darmstadt, Germany, 1998, vol. 9, no. 11. [Online]. Available: http://ftp.aiub.unibe.ch/ionex/draft/ionex11.pdf

[29] R. Bamler and M. Eineder, "Accuracy of differential shift estimation by correlation and split-bandwidth interferometry for wideband and Delta-k SAR systems," *IEEE Geosci. Remote Sens. Lett.*, vol. 2, no. 2, pp. 151–155, Apr. 2005, doi: 10.1109/LGRS.2004.843203.

Felipe Betancourt-Payan (Graduate Student Member, IEEE) was born in Armenia, Quindio, Colombia, in 1993. He received the bachelor's degree in aerospace engineering from Carlos III University, Madrid, Spain, in 2017, and the master's degree in space science and technology (SpaceMaster) from Luleå University of Technology, Luleå, Sweden, and Universite Toulouse III-Paul Sabatier, Toulouse, France, in 2019. He is currently pursuing the Ph.D. degree with the German Aerospace Center (DLR-HR), Weßling, Germany.

Since 2019, he has been with the Microwaves and Radar Institute, German Aerospace Center (DLR-HR). His research interests include using autofocus techniques for ionospheric correction and retrieving ionospheric parameters from low-frequency synthetic aperture radar (SAR) images.

Marc Rodriguez-Cassola was born in Barcelona, Spain, in 1977. He received the Ingeniero degree in telecommunication engineering from the Universidad Publica de Navarra, Pamplona, Spain, in 2000, the Licenciado (M.Sc.) degree in economics from the Universidad Nacional de Educacion a Distancia, Madrid, Spain, in 2012, and the Ph.D. degree in electrical engineering from Karlsruhe Institute of Technology, Karlsruhe, Germany, in 2012.

From 2000 to 2001, he was a Radar Hardware Engineer with the Study Center of Terrestrial and Planetary Environments (CETP)/French National Center for Scientific Research (CNRS), Saint-Maur-des-Fossés, France. From 2001 to 2003, he was a Software Engineer with Altran Consulting, Munich, Germany. Since 2003, he has been with the Microwaves and Radar Institute, German Aerospace Center, Weßling, Germany, where he is leading the SAR Missions Group. His research interests include radar signal processing, synthetic aperture radar (SAR) end-to-end simulation, SAR processing and calibration algorithms, crisis theory, and radar mission analysis and applications.

Pau Prats-Iraola (Fellow, IEEE) was born in Madrid, Spain, in 1977. He received the Ingeniero and Ph.D. degrees in telecommunications engineering from the Universitat Politècnica de Catalunya (UPC), Barcelona, Spain, in 2001 and 2006, respectively.

In 2001, he joined the Institute of Geomatics, Barcelona, as a Research Assistant. In 2002, he joined the Department of Signal Theory and Communications, UPC, where he worked in the field of airborne repeat-pass interferometry and airborne differential synthetic aperture radar (SAR) interferometry. From December 2002 to August 2006, he was an Assistant Professor with the Department of Telecommunications and Systems Engineering, Universitat Autònoma de Barcelona, Barcelona. In 2006, he joined the Microwaves and Radar Institute, German Aerospace Center (DLR), Weßling, Germany, where he has been the Head of the Multimodal Algorithms Group, since 2009. He is the responsible and a Main Developer of the TanDEM-X interferometric (TAXI) processor, an end-to-end processing chain for data acquired by the TerraSAR-X and TanDEM-X satellites, which has been used to demonstrate novel SAR acquisition modes and techniques. He is currently involved in the design and implementation of ground processor prototypes and end-to-end simulators of ESA's BIOMASS and ROSE-L missions. His research interests include high-resolution airborne/spaceborne monostatic/bistatic SAR processing, SAR interferometry, advanced interferometric acquisition modes, persistent scatterer interferometry (PSI), SAR tomography, and end-to-end SAR simulation. He has co-authored more than 60 peer-reviewed journal articles in these fields.

Gerhard Krieger (Fellow, IEEE) received the Dipl.-Ing. (M.S.) and Dr.-Ing. (Ph.D.) (Hons.) degrees in electrical and communication engineering from the Technical University of Munich, Munich, Germany, in 1992 and 1999, respectively.

From 1992 to 1999, he was with Ludwig Maximilians University, Munich, where he conducted multidisciplinary research on neuronal modeling and nonlinear information processing in biological and technical vision systems. Since 1999, he has been with the Microwaves and Radar Institute, German Aerospace Center (DLR), Weßling, Germany, where he started as a Research Associate, developing signal processing algorithms for a novel forward-looking radar system employing digital beamforming on receive. From 2001 to 2007, he led the New SAR Missions Group, Wessling, which pioneered the development of advanced bistatic and multistatic radar systems, such as TanDEM-X, as well as innovative multichannel synthetic aperture radar (SAR) techniques and algorithms for high-resolution wide-swath SAR imaging. Since 2008, he has been the Head of the Radar Concepts Department, Wessling, which hosts about 40 scientists focusing on new SAR techniques, missions, and applications. He has been serving as a Mission Engineer for TanDEM-X, and he also made major contributions to the development of the Tandem-L mission concept, where he led the Phase-0 and Phase-A studies. Since 2019, he has also been holding a professorship at Friedrich-Alexander University Erlangen–Nuremberg (FAU), Erlangen, Germany. He has authored or co-authored more than 100 peer-reviewed journal articles, nine invited book chapters, and more than 400 conference papers, and holds more than 20 patents.

Prof. Krieger has been an Associate Editor of IEEE TRANSACTIONS ON GEOSCIENCE AND REMOTE SENSING since 2012. In 2014, he served as the Technical Program Chair for the European Conference on SAR and a Guest Editor for IEEE JOURNAL OF SELECTED TOPICS IN APPLIED EARTH OBSERVATIONS AND REMOTE SENSING. He received several national and international awards, including two best paper awards at the European Conference on SAR, two transactions prize paper awards from the IEEE Geoscience and Remote Sensing Society, and the W.R.G. Baker Prize Paper Award from the IEEE Board of Directors.